

# The Nova Synthetic Data Base: a PCA/AI Analysis of Novae Synoptic Spectra

BRUNO C. SANTOS,<sup>1</sup> MARCOS P. DIAZ,<sup>1</sup> AND LARISSA TAKEDA<sup>1</sup>

<sup>1</sup>*Instituto de Astronomia, Geofísica e Ciências Atmosféricas da Universidade de São Paulo (IAG-USP)*

*Rua do Matão, 1226, Cidade Universitária  
05508-090 São Paulo, SP Brazil*

(Dated: April 30, 2026; Accepted March 09, 2026; Published April 30, 2026)

Submitted to The Astrophysical Journal Supplement Series

## ABSTRACT

The Nova Synthetic Data Base (NSDB) is presented as the first publicly available database of synthetic spectra for classical nova shells, spanning an unprecedented range of physical parameters (e.g., ejecta mass, chemical composition, temperature, and luminosity of the white dwarf) at several post-eruption ages. Generated using detailed 3D photoionization models, this homogeneous database enables a systematic exploration of spectral features in novae. In this work, we introduce a PCA/AI-based framework to derive time-dependent proxies for retrieving the physical properties of novae from limited spectral data. By analyzing the correlations between the eigen-spectra and the grid's variables, a reduced set of diagnostic spectral lines is derived, paving the way for robust multi-regressor machine-learning algorithms with a minimal effort observational set. The prediction capability of the method is high and robust to data noise. The results establish a proof of concept for the use of model grids combined with physically controlled AI as a tool to interpret novae observations in the context of the large number of events expected from future wide area surveys.

*Keywords:* Classical novae (251), Photoionization (2060), Near infrared astronomy (1093), Near ultraviolet astronomy (1094), Optical astronomy (1776), Spectroscopy (1558), Multivariate analysis (1913), Dimensionality reduction (1943), Principal component analysis (1944), Random Forests (1935), Regression (1914), Astronomy databases (83)

## 1. INTRODUCTION

Cataclysmic variables are binary systems in which the secondary component transfers mass to a white dwarf. This interaction between stellar components leads to

unique observational signatures, one of which being among the most energetic stellar phenomena in the Universe: classical novae. The accretion of material onto the degenerate primary builds up a hydrogen-rich layer, eventually triggering a thermonuclear runaway (TNR). This results in a recurrent eruption, ejecting shells that expand at velocities of  $\sim 10^3 \text{ km s}^{-1}$  and a range of mass loss of  $10^{-7} - 10^{-4} M_{\odot}$  per event. Chemical signatures from both the primary and secondary, along with the products from TNR nucleosynthesis, are returned to the ISM (Warner 1995). Beyond being theorized as potential progenitors of Type Ia Supernovae, these systems play an important role in synthesizing  ${}^7\text{Li}$  and rare isotopes (Starrfield et al. 1978). Their study is important for understanding the details of galactic chemical evolution (Borisov et al. 2024) and for constraining the Single Degenerate progenitor channel (Maoz et al. 2014) of Type Ia Supernovae. Improving our knowledge of these progenitors is, in turn, a key step toward further refining the most widely used method for determining cosmological distances (Perlmutter et al. 1999; Riess et al. 1998).

Observed nova spectra diverge significantly from those depicted by one-dimensional photoionization models with acceptable physical parameters. The simultaneous presence of spectral lines of neutral elements and highly ionized species at several post-eruption ages (Williams 1992), along with the large optical depth of lines like [O I], can only be explained by high-density mass clumps embedded in the diffuse plasma during the nebular phase (Williams 1994; Diaz et al. 2010). Spatially resolved observations of nova shells (Slavin et al. 1995; Moraes & Diaz 2009; Diaz et al. 2018) clearly show a complex structure and the presence of mass clumps in classical nova ejecta.

Various three-dimensional modeling efforts of ionized nebulae have been attempted at high computational cost (e.g. Gruenwald et al. 1997; Ercolano et al. 2003). In this context, a three-dimensional approach for modeling the nebular anisotropic medium was proposed in the photoionization code RAINY3D (M. Moraes 2011, see also Section 2.1). Previous works have demonstrated the capability of this approach to replicate the physical environment of classical novae in the nebular phase. Takeda et al. (2018) presented a dive into the slow novae *V723 Cas* photoionization structure, showing that more realistic anisotropic mass and radiation field distributions are critical for reproducing the system’s complex features, unlike simplistic 1D approaches.

The forthcoming increase in public spectroscopic novae data (e.g., VRO, ZTF-BTS) will soon overwhelm our efforts in individual modeling, while opening unprecedented nova population and evolution studies if basic parameters can be obtained directly from the observed spectrum. In this context, the qualitative classification scheme of Williams et al. (1991) - based on emission line evolution and observable properties - pioneered the systematic observational framework of novae categorization and correlation of spectral properties with global parameters, i.e. mean mass gas density and ionizing radiation field. Machine learning methods trained on synthetic model

grids offer a promising follow-up alternative, but only if spectral features can be unambiguously and quantitatively mapped to specific physical parameters.

In this paper, we present a **Principal Component Analysis** (PCA) of the large NSDB 3D synthetic spectral grid for classical novae: the *Nova Synthetic Data Base*. This grid comprises 1439 models (875 for the CO nova grid, 564 for the Ne enhanced nova grid) of anisotropic shells, with condensed mass clumps added to a symmetric power-law background, spanning a wide range of physical parameters. By identifying correlations between the eigenspectra and the physical parameters, we were able to identify sets of diagnostic spectral lines that act as time-dependent proxies for the shell and central source properties. This framework not only enables rapid parameter ranging from incomplete observational data but also sets the stage for AI-driven analyzes. PCA preliminary analysis favors a closer physical insight into the AI methods and their application to next-generation nova synoptic data, without the need for single-object photoionization modeling.

## 2. METHODOLOGY

### 2.1. *The Nova Synthetic Data Base*

The *Nova Synthetic Data Base* is a synthetic spectral database of nova shells at several evolutionary stages. The grid is defined by 6 basic free parameters, which we believe represent the most relevant physical properties of the classical novae photoionization scenario, namely the post-Nova age, ejected mass, condensed mass-fraction, C,N,O abundance, luminosity, and temperature of the central source. Two separate similar grids are available, one of them is calculated using typical neon nova enhanced Ne abundance.

The C, N, and O content is varied with fixed fractions by  $\pm 1$  dex around averaged nova values, mostly taken from [Gehrz et al. \(1998\)](#) compilation ( $\log N_{C,N,O}/N_H = -2.06, -1.847, -1.77$ ). Solar abundances ([Asplund et al. 2009](#)) were assumed for all elements other than He, C, N, O, and Ne for the neon nova grid. Nova ejected masses ranging from  $8 \times 10^{-6}$  to  $10^{-4} M_{\odot}$  are intended to cover the most commonly observed values in classical novae regime. The post-eruption ages between 80 – 2560 days focus on the nebular phase of fast ejected shells. This initial version of the model grid assumes a constant expansion velocity profile, with effective velocities of 1500, 950, and 400  $km s^{-1}$  as maximum, average, and minimum velocities, completely coupling the inner and outer radii as well as the mean density of the simulated shell with the post-eruption age. Consequently, slower or even faster novae may find their place in the grid by scaling their post-eruption age. The shell is assumed to have a constant velocity expansion for the radiative transfer. The central source properties also aim to cover values often reported in the literature for classical novae. Its SED is simulated from high-gravity hot NLTE spectra by ([Rauch 2003](#)). More details are given in [Table 1](#).

**Table 1.** NSDB Grid Input Parameters

Parameters	Minimum Value	Maximum Value	Number of Values
Age	80 <i>days</i>	2560 <i>days</i>	6
Ejected Mass (M)	$8 \times 10^{-6} M_{\odot}$	$1 \times 10^{-4} M_{\odot}$	3
Condensed fraction (fc)	0.2	0.8	4
Luminosity (log(L))	36.5	38.5	3
Temperature (T)	$1 \times 10^5$ K	$3.5 \times 10^5$ K	3
C,N,O abundance (log $N_x/N_H$ )	-3.06,-2.847,-2.77	-1.06,-0.847,-0.77	2

NOTE—This table summarizes the parameter ranges and the number of values sampled for each parameter, with luminosity in CGS units. Models of age 2560 days do not include the highest central source luminosity value. The CO Grid adopts solar Ne abundance, whereas the Neon Grid adopts  $\log N_{Ne}/N_H = -2.07$ .

Paving the way for a systematic exploration of the spectral signatures of condensations, a range of 20% to 80% condensed mass-fraction relative to total mass (fc) is assumed. Less changes in the resulting spectrum are seen beyond these limits because higher values lead to shells where the gaussian condensation tails blend with the diffuse power-law component and with each other, whereas lower values result in spectra dominated by emission from the symmetric component. There are very few constraints on the mass fraction in the literature. The work by [Abraham et al. \(2024\)](#) indicates  $fc \sim 0.4$  for the shell around nova V5668 Sgr. The condensation radius (FWHM) is a fixed fraction (1/8) of the shell outer radius, while their peak density contrast relative to the diffuse background is 20; values inspired by the ALMA imaging of V5668 Sgr ([Diaz et al. 2018](#)). The symmetric radial power-law background has an index of -1.4 for CO novae and -1.0 for neon novae. These values were roughly estimated from the  $H\alpha$  emissivity fitting and deprojection of a few resolved shells. The integrated spectrum depends weakly on the power-law index, given that the inner radius of the shell is a significant fraction of the shell thickness.

The models were constructed using the anisotropic photoionization code RAINY3D ([M. Moraes 2011](#)). The code builds an expanding shell with two mass distribution components: a radially symmetric power-law and gas clumps with Gaussian contrast density profiles and sizes, both of which may be governed by power-law probability functions. However, they were predefined in the present grids instead. Random clump positions, embedded in the spherically symmetric background, are assumed. The condensed mass-fraction parameter (fc) is more appropriate than filling or covering factors when comparing clumpy models with different density contrasts. Once the anisotropic shell is defined, the photoionization code CLOUDY ([Ferland et al. 2013](#))

is called as a subroutine to calculate the 1D photoionization and thermal equilibrium, as well as the radial radiative transfer of the white dwarf’s and diffuse radiation fields. RAINY3D has a feature to include an accretion disk contribution to the radiation field, parameterized by the accretion rate and the white dwarf mass; a feature that was not used in the presented results.

As an output of every model, RAINY3D provides local and integrated line fluxes, accounting for the entire shell, of 241 selected spectral lines of different elements at several ionization stages, which compose possible nova remnant spectra. Calculated line fluxes correspond to observed values at a distance of 1.0 kpc in the absence of extinction. The line list was selected on the basis of Cloudy’s atomic lines database and on the lines that are commonly found in nova visible and NIR spectra available in the literature. A rest wavelength range from  $\lambda 3200 \text{ \AA}$  to  $\lambda 24,800 \text{ \AA}$  (from near-UV to NIR) was chosen; the full spectral line selection can be found at [Appendix A](#).

The grid was entirely computed using the Santos Dumont (SDumont) supercomputer facility at the Laboratório Nacional de Computação Científica (LNCC), with a hybrid CPU architecture and a peak performance of 5.1 PetaFLOPs.

Ultimately, 875 novae remnants models compose the final CO novae grid, described by 241 total line fluxes per model, covering the optical to near-infrared wavelengths. This grid is a homogeneous dataset where individual model structures, including local emissivities and physical conditions, can be retrieved. An enhanced neon grid was also computed, aiming to model the neon nova spectral evolution. The NSDB data are publicly available at the IAG-USP model repository: <http://specmodels.iag.usp.br>.

## 2.2. Line Fluxes and Variable Spaces

Before detailing the method of analysis of this extensive data set, we first define the variable spaces that will be treated: The most direct variables that map the world of models are the input variables of RAINY3D (listed in [Table 1](#)). This mapping is called *Parameter-Space*, which describes the 875 CO models through the 6 input parameters of the code used to create the grid.

Another way to represent the computed shells is through the resulting integrated line flux sets. Each spectrum was normalized by its  $H\beta$  ( $\lambda\lambda 4861.33 \text{ \AA}$ ) value, resulting in the *Spectral-Space*. This space maps the world of models through 240 selected line fluxes relative to  $H\beta$ . These lines are or may be observed in nova ejecta at all ages. In this space, the eigenvalues and eigenspectra decomposition will be performed in order to find a representation base, eigenspectra, which better describes the variance of line fluxes within each age subset.

Aiming to construct the representation base, the 100 brightest spectral lines were extracted from our previously selected list in order to minimize noise from stochastic variable realization and statistical fluctuations introduced by RAINY3D’s pseudo-random processes while avoiding, as much as possible, the use of lines that cannot be observed at moderate signal-to-noise ratios (despite their potential diagnostic power).

Therefore, this selection criterion prioritizes lines with the highest flux ratios relative to  $H\beta$ .

The dataset subjected to this selection is the epoch-wise spectral space, or the 100 main spectral lines that better describe each post-eruption age. This will be the *Epoch-Selection*, built for each of the 6 post-eruption ages modeled. All 6 spectral line selections are presented in [Appendix B](#).

### 2.3. PCA Decomposition

Dealing with computed models (i.e. without observational biases, incomplete sampling, stochastic noise, and extinction correction uncertainties), it is recommended to perform the eigenvalues-eigenvectors decomposition directly on a homogeneous *data correlation matrix* (Murtagh & Heck 2012): the line flux sample is centralized and scaled to unit variance (standardization/Z-score) for each Spectral-Space’s variable (selected spectral lines). In addition, the sample is normalized by the number of models considered. This creates a space where the distance between variables is proportional to their correlation, preserving the weight of weak line relative variance. Once the decomposition of the data correlation matrix is performed, the eigenspectra are ranked by their cumulative explained variance. A 90% threshold is adopted to ensure the capture of the primary physical-related signal while effectively filtering out noise and most uncertainties intrinsic to integrated line luminosity from observations.

It is worth mentioning that we expect the decomposition to retrieve a number of eigenvectors similar to or greater than the hidden variables of the Parameter-Space (5 per age). A smaller number of axes would mean that some physical variable used to construct the model’s grid is degenerate or fully correlated with another variable.

With the decomposition method at hand, it may be applied to various synthetic spectra datasets along with their respective line selections. As a result, 6 eigenspectra were obtained, with the number of eigenvectors per base varying from 5 to 9 for the Epoch-Selections. Each eigenvector in these eigenspectra is a vector with 100 components, which represents, in its absolute value, the relative contribution of the corresponding spectral line to that eigenvector.

Mathematically, these eigenspectra define a new orthogonal basis that maximizes the variance of the model ensemble, providing vectors (or axes) that better map and describe the dataset.

### 2.4. Variables Correlation & Diagnostic Lines

To explore possible correlations between the PCA-derived basis and the fundamental novae physical parameters, the standardized data are projected onto the new basis, and the *variables correlation matrix* is computed: This matrix contains Pearson correlation coefficients between the [eigenspectra](#) obtained and the [Parameter-Space](#) input variables, calculated using the *corrwith* method from the Pandas library (McKinney 2010; [The pandas development team 2023](#)).

Searching for significant correlations, we were able to predict, among the 100 brightest expected spectral lines in the optical and near-infrared ranges, the most useful diagnostic lines for each age. Diagnostic lines show a greater relative contribution to eigenspectra and correlation with physical parameters. Defining a minimum absolute correlation of 0.25 with any physical variable, the diagnostic significance of a spectral line for the diagnosis of that variable is calculated using the following formula:

$$I_{i,k} = \sum_j ES_i^j \times |corr(ES^j, V_k)| \times P_j ; \quad (1)$$

where the importance of the spectral line  $i$  for the diagnosis of the variable  $k$ ,  $I_{i,k}$ , is given by the sum of its contribution to the  $j$ -th eigenspectra,  $ES_i^j$ , weighted by the absolute correlation of that eigenspectra with the variable under analysis and by the percentage of total variance explained by the  $j$ -th eigenspectra  $P_j$ . The last weighting term is justified by both preserving the quality ranking in the description of generic novae spectra and reducing the influence of spurious correlations and noise in the analysis, which is critical when an application to observed spectra is intended.

### 2.5. Machine Learning Application

Aiming to establish robust diagnostics of nova spectra, an AI-based algorithm should be able to inversely map spectral features to physical parameters using only the most relevant diagnostic lines derived from PCA analysis. For this reverse prediction task, we implemented a *Random Forest* (Breiman 2001) regressor based on three critical properties:

- *Bootstrap aggregation*: each tree trains on randomized data subsets (with replacement), maximizing information extraction from a limited model grid.
- *Double randomness* mechanism - random data subsets per tree and random feature subsets at node splits - minimizes tree correlations and, therefore, mitigates *overfitting*.
- This architecture accepts *transfer learning* techniques for future applications to observed data.

Considering that tree-based regressors perform poorly in extrapolating beyond the training range, our model's grid was designed to cover the most common physical parameter space of classical novae.

To ensure reliable diagnostics, we require a homogeneous set in the Parameter-Space. For this purpose, and because of the lack of convergence of some models in the two earliest epochs, the subsets with age in the range of 320 - 2560 days were selected.

For the hyperparameter optimization, different regressors were evaluated using the *mean absolute error* (MAE) metric, exploring eight optimization parameters of the

Random Forest Regressor ensemble, as available in the Scikit-learn library (Pedregosa et al. 2011): the number of trees (with a minimum number of 100 to ensure at least one usage of each spectral line selected in a random-walk-like selection process), maximum features per tree, maximum tree depth, minimum samples per leaf node, minimum samples for node splitting, and three other secondary parameters accounting for the split loss function, minimum impurity decrease per division, and pruning complexity parameter. The search employed 5-fold cross-validation with randomized partitioning, following established best practices for astrophysical machine learning applications (Ivezić et al. 2019).

After establishing the best model, we evaluate its performance using two complementary approaches:

- (1) The *out-of-bag* (OOB) score - an intrinsic Random Forest metric based on bootstrap aggregation, where each tree is evaluated on unseen data from its training set. This provides an estimate of the model’s generalization without requiring a separate validation data set.
- (2) Parameter-Space specific metrics, including MAE and  $R^2$  *coefficient of (multiple) determination* - interpreted as the fraction of a variable variance explained by the model and are widely used as a first adequacy indicator for any multiple regression model (Devore 2011, Cap. 13).

These metrics were computed epoch-wise to account for evolutionary dependencies in our database.

The optimization and evaluation are repeated for a decreasing number of diagnostic lines, building regressor models for the top  $n$  most relevant diagnostic lines according to the PCA analysis described above. The smaller  $n$ , while achieving satisfactory retrieval of physical parameters, represents the minimum observational effort and greater dimensionality reduction.

### 2.6. Simulating Observations

As a final test of the method, Gaussian noise is applied to the Spectral-Space, simulating observational data of Novae in preparation for future applications of the framework constructed here. One-sigma uncertainties are applied to the simulated flux, from 0% up to 20% of the flux, and a hundred realizations are made to achieve statistical relevance at each uncertainty level. The final evaluation metrics are then computed for each bootstrap.

The performance evaluation against noisy data follows specific metrics to account for different ranges, sampling, and performance differences in Parameter-Space. The absolute relative error is derived for the linear grid variables, namely the ionizing source temperature and the condensed mass fraction of the envelope, while the absolute logarithmic error is calculated for logarithmic grid variables such as the ejected mass, C,N,O abundance, and central source luminosity. The median central value is

**Table 2.** Eigenspectra Decomposition

Age ( <i>days</i> )	no. of Eigenspectra	Maximum Variance Explained	Minimum Variance Explained
80	5	50.0%	3.9%
160	5	43.1%	4.9%
320	9	25.9%	2.5%
640	9	28.8%	2.4%
1280	8	30.6%	2.5%
2560	6	36.8%	4.9%

NOTE—Number of eigenvectors necessary to achieve 90% of Spectral-Space’ variance and their maximum and minimum eigenvectors’ explained variance for each age using the Epoch-Selection lines.

computed for each physical parameter. The *MAPE* and *MALE* define an uncertainty-like metric, in percentage and in dex, for our regressor model. They grade the retrieval of Nova physical parameters from limited spectroscopic data.

### 3. RESULTS & DISCUSSION

Firstly, we present the 6 eigenspectra decomposition using the [Epoch-Selection](#) in [Table 2](#). Notably, the model spaces for the two earliest post-eruption epochs (80 and 160 days) and the latest (2560 days) are well described by only five and six eigenspectra, respectively – 3 or 4 fewer than required for intermediate epochs. This is directly linked to the reduced physical parameter space of these subsets. At the early stages, unstable models were disregarded from the model grid. For the latest epoch, the highest white dwarf luminosity is physically excluded, as the central source has possibly cooled by that time. These limitations create reduced ranges at these epochs. Consequently, the number of models drops from 217 to 37 at 80 days, 46 at 160 days, and 144 at 2560 days. This reduction in input parameters within the [Parameter-Space](#) enhances the correlations between the eigenspectra and these critical variables, as detailed in [Table 3](#).

A global line selection (accounting for all post-Nova ages) was attempted, requiring more eigenvectors to reach the 90 variance threshold without bringing any gain in the correlations between the input parameters (including post-eruption age) and these eigenvectors. This reflects the complexity of spectral evolution in novae and suggests that post-eruption age, which defines size scales and densities, is an essential observable that defines the diagnostic framework. We therefore focus on the Epoch-Selection, which achieves significant dimensionality reduction – compressing

the [Spectral-Space](#) from 100 spectral lines to 5–9 eigenspectra while preserving diagnostic power.

### 3.1. *Eigenspectra & Correlations*

As outlined in [Section 2.3](#), each eigenspectra composing the basis is a vector whose components represent the absolute contribution of the corresponding spectral line to that eigenvector, given the post-eruption age and the emission line sample. These contributions arise from the variance (in standard deviation units) of each spectral line ratio across age-specific model sets and their diagnostic power in discriminating models with varying physical parameters.

[Figure 1](#) illustrates representative eigenspectra, plotted as delta functions at their respective wavelengths. Both figures show general features present in all post-eruption ages:

1. Dominant eigenspectra (those explaining the most variance - represented by [Figure 1](#) top panels) are overwhelmingly dominated by He lines (neutral and ionized), with consistent but secondary contributions from H lines. Highly ionized metals (e.g., Ca v, Ar v, Fe VII) become increasingly prominent in these components beyond 640 days. The distribution between optical and NIR lines varies with age, showing no trend or clustering.
2. Minor eigenspectra primarily feature optical-region lines from highly ionized metals (e.g., Fe VI, Fe VII, N IV, Ne v, O IV, Ar v), though NIR features (e.g., Al IX) appear in specific eigenvectors. Their significance seems age-dependent, peaking at intermediate evolutionary stages (160–1280 days).

This scenario is aligned with the expected nebular line formation ([Osterbrock & Ferland 2006](#)) and PCA’s discrimination. The overall ionization structure of the envelope can be found through the analyzes of H, He I and He II lines, giving rise to their large contribution in the main eigenspectra - The migration of ionized metals (e.g. Ar v/Fe VII) into these dominant components at late ages reflects a shift in the ionization regime of the remnants. The contribution of ionized metal lines’ in minor eigenspectra is a consequence of their diagnostic power between similar models, enabling fine mapping within [Spectral-Space](#).

With the eigenspectra at hand, the correlation between these newly derived axes and the input variables of the [Parameter-Space](#) - the critical physical variables for the construction of the [Nova Synthetic Data Base](#) - can be pursued.

[Table 3](#) compiles peak correlations between parameters and age-specific eigenspectra using the Epoch-Selection. All parameters, except fc (mass fraction in condensations), show significant correlations ( $\gtrsim 0.3$ ) across epochs. The low correlation values for fc across all epochs are noteworthy. While a purely statistical approach might suggest a negligible role for this parameter, the physical significance of condensations has been extensively demonstrated (e.g., [Williams 1994](#); [Diaz et al. 2010](#)). Moreover, the

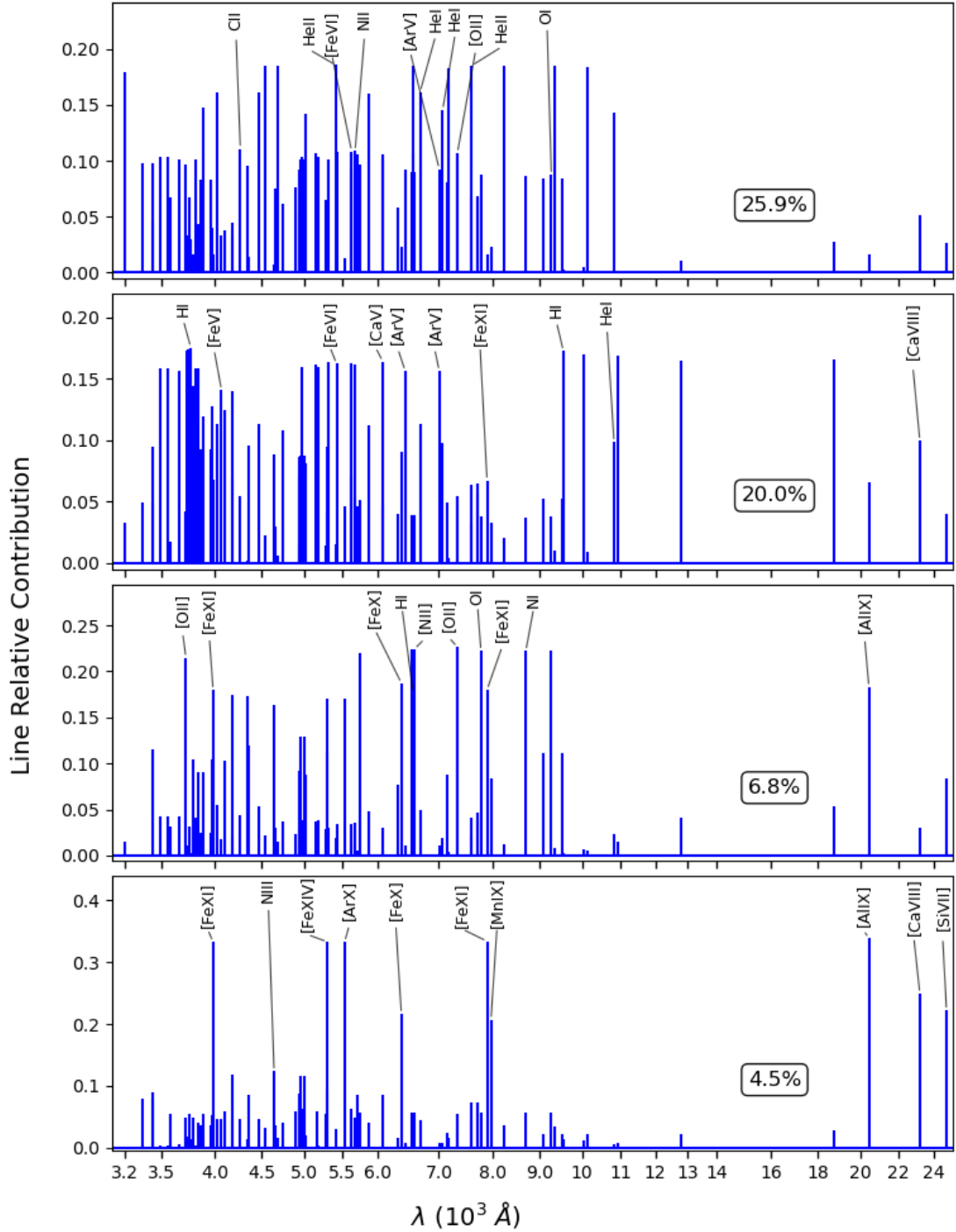


**Figure 1.** Line relative contribution to variance of the, from top to bottom, higher representative eigenspectra 1 and 2, and lower eigenspectra 5 and 7, at 320 days post-eruption using the Epoch-Selection, with their respective variance explained as percentages. The black tags label the top line ratio of the 5 most important ions in the visible (< 7000  $\text{\AA}$ ) and the 5 most important ions in the NIR (> 7000  $\text{\AA}$ ), ranked by their contribution in each case. Wavelength axis in log scale.

**Table 3.** Maximum Correlation Coefficients for Epoch-Selection

Parameter	80 <i>days</i>	160 <i>days</i>	320 <i>days</i>	640 <i>days</i>	1280 <i>days</i>	2569 <i>days</i>
M	0.47	0.40	0.50	0.36	0.27	0.43
fc	0.26	0.10	0.04	0.05	0.04	0.06
L	0.60	0.68	0.46	0.38	0.38	0.44
T	0.70	0.65	0.78	0.75	0.70	0.89
C,N,O abundance	-/-	-/-	0.64	0.65	0.62	0.67

NOTE—Maximum (absolute) correlation coefficients between the variables in the Parameter-Space and the eigenspectra of each age. Models of age 80 and 160 days does not include C,N,O abundance as a variable.

application of the RAINY3D approach in previous spectral syntheses (e.g. [Takeda et al. \(2018\)](#)) supports the view that fc is a critical, albeit complex, driver of the spectral evolution in nova remnants. The low correlation indicates that the spectral response to high density clumps cannot be simplified into few linear components, unlike the more straightforward responses to parameters like effective temperature, luminosity, or ejected mass.

### 3.2. *Novae Diagnostic Spectral Lines*

The significant correlations between Parameter-Space variables and eigenspectra for each age (see [Table 3](#)) enable the identification of the main diagnostic spectral lines for each parameter. Using [Equation \(1\)](#), we calculate the percentage relevance of spectral lines for each variable; below we have compiled the *top 10 diagnostic spectral lines* within the Spectral-Space epoch-wise:

For better visualization, we group the 241 spectral lines of RAINY3D into 8 categories and compute their percentage of importance: H I, He I and He II; Neutral C,N,O lines; Coronal lines including [Fe XIV] ( $\lambda 5303.01$ ), [Ar X] ( $\lambda 5534.02$ ), [Ca VIII] ( $\lambda 23211.7$ ), among others; Classic Diagnostic [O III], [N II], and [S II] as electron temperature and density diagnostic lines; and Other Forbidden, accounting for forbidden lines not already accounted for.

[Tables 5](#) reveals a clear dominance of H and He lines in diagnosing Parameter-Space variables as a direct result of the PCA methodology employed. As discussed in [Section 3.1](#), H and He recombination lines often dominate the optical spectral features in nova shells and nebulae. Since PCA prioritizes global variance patterns within the

**Table 4.** Top 10 Diagnostic Lines: Early and Late Post-Eruption Ages

Rank	80 days	160 days	320 days
1	H I ( $\lambda\lambda 9545.93$ )	He I ( $\lambda\lambda 6678.15$ )	He II ( $\lambda\lambda 5411.37$ )
2	He I ( $\lambda\lambda 7065.22$ )	He I ( $\lambda\lambda 5015.68$ )	He II ( $\lambda\lambda 10123.3$ )
3	H I ( $\lambda\lambda 19445.4$ )	He II ( $\lambda\lambda 3923.37$ )	H I ( $\lambda\lambda 3770.63$ )
4	H I ( $\lambda\lambda 9014.87$ )	He I ( $\lambda\lambda 5875.64$ )	[Fe VII] ( $\lambda 3586.32$ )
5	He I ( $\lambda\lambda 4713.03$ )	[Ne III] ( $\lambda 3868.76$ )	He II ( $\lambda\lambda 6559.91$ )
6	He I ( $\lambda\lambda 5875.64$ )	He II ( $\lambda\lambda 3857.96$ )	H I ( $\lambda\lambda 3750.15$ )
7	[Ne III] ( $\lambda 3868.76$ )	He I ( $\lambda\lambda 4921.93$ )	[Fe VII] ( $\lambda 3758.92$ )
8	N V ( $\lambda\lambda 4945.0$ )	[Ne III] ( $\lambda 3967.47$ )	He II ( $\lambda\lambda 9344.62$ )
9	He I ( $\lambda\lambda 6678.15$ )	He II ( $\lambda\lambda 6682.98$ )	H I ( $\lambda\lambda 3734.36$ )
10	[Ne III] ( $\lambda 3967.47$ )	He I ( $\lambda\lambda 4471.49$ )	[Fe VII] ( $\lambda 5276.38$ )
Rank	640 days	1280 days	2560 days
1	He II ( $\lambda\lambda 3923.37$ )	He II ( $\lambda\lambda 10123.3$ )	[Fe VII] ( $\lambda 4942.48$ )
2	He II ( $\lambda\lambda 4541.46$ )	H I ( $\lambda\lambda 4340.46$ )	He II ( $\lambda\lambda 3923.37$ )
3	He I ( $\lambda\lambda 6678.15$ )	H I ( $\lambda\lambda 10938.0$ )	[Ar V] ( $\lambda 6435.12$ )
4	C IV ( $\lambda\lambda 4659.0$ )	C IV ( $\lambda\lambda 4659.0$ )	[Fe VII] ( $\lambda 5276.38$ )
5	He II ( $\lambda\lambda 3857.96$ )	He II ( $\lambda\lambda 6559.91$ )	He II ( $\lambda\lambda 6682.98$ )
6	H I ( $\lambda\lambda 19445.4$ )	H I ( $\lambda\lambda 6562.81$ )	[Ar V] ( $\lambda 7005.83$ )
7	He I ( $\lambda\lambda 4471.49$ )	He II ( $\lambda\lambda 5411.37$ )	[Fe VII] ( $\lambda 4988.55$ )
8	[Ar V] ( $\lambda 6435.12$ )	[Ar V] ( $\lambda 7005.83$ )	He II ( $\lambda\lambda 10123.3$ )
9	He II ( $\lambda\lambda 6682.98$ )	He II ( $\lambda\lambda 4685.64$ )	[Ca V] ( $\lambda 5309.11$ )
10	H I ( $\lambda\lambda 21655.1$ )	N III ( $\lambda\lambda 4641.0$ )	[Fe VII] ( $\lambda 3586.32$ )

NOTE—Top diagnostic lines ranked by importance for post-eruption ages within the NSDB. Upper panel shows early ages with transition from hydrogen/helium dominated to higher ionization species. Lower panel shows late ages with increased dominance of high-ionization species and iron. An extended version of this table is available at the database website.

dataset, H and He lines naturally dominate the mapping. Considering the emission process, there is a redundancy in the recombination transitions at low densities. However, the local emission roughly scales with the square of the density, being dominated by the highest density regions in the condensations and/or inner shell. In this case, self absorption is expected to be significant, and standard decrements are no longer

**Table 5.** Percentage Contribution of Main Diagnostic Lines

Line Type	80d (%)	160d (%)	320d (%)	640d (%)	1280d (%)	2560d (%)
<i>Mass</i>						
H I	25.7	19.2	8.2	21.7	26.2	16.5
He I	15.4	20.1	11.9	6.6	5.3	8.2
He II	15.2	21.9	18.8	22.7	27.7	7.8
Neutral C,N,O	0.0	0.0	2.5	0.0	0.0	0.0
Coronal	6.9	4.3	3.0	2.3	2.1	10.9
Classic Diagnostic	3.4	6.3	4.4	2.2	1.6	2.9
Other Forbidden	12.6	12.9	16.9	11.8	8.6	12.5
<i>Abundance</i>						
H I	–	–	16.8	17.2	16.1	28.8
He I	–	–	3.2	3.6	8.4	5.4
He II	–	–	6.2	7.4	7.1	15.0
Neutral C,N,O	–	–	2.1	0.0	0.0	0.0
Coronal	–	–	6.5	6.9	6.7	3.3
Classic Diagnostic	–	–	4.8	1.9	2.7	2.8
Other Forbidden	–	–	21.8	18.9	17.7	14.6
<i>Luminosity</i>						
H I	24.9	15.3	10.2	22.9	23.0	16.5
He I	14.5	16.3	9.7	8.8	11.9	8.2
He II	14.2	16.9	15.2	17.4	5.7	7.8
Neutral C,N,O	0.0	0.0	2.6	0.0	0.0	0.0
Coronal	6.4	5.6	3.9	4.0	7.5	10.9
Classic Diagnostic	3.1	6.0	4.6	4.1	5.1	2.9
Other Forbidden	13.3	15.7	18.4	12.1	14.3	12.5
<i>Temperature</i>						
H I	25.1	20.7	23.1	26.0	26.4	37.3
He I	17.5	14.4	10.2	12.5	9.6	0.9
He II	18.1	18.9	1.9	18.4	21.3	27.7
Neutral C,N,O	0.0	0.0	1.4	0.0	0.0	0.0
Coronal	5.0	5.0	5.8	3.0	2.6	3.7
Classic Diagnostic	3.4	4.7	4.2	5.0	3.6	1.2
Other Forbidden	11.3	13.7	19.5	10.8	9.9	7.7

followed. The intensities in all series are properly calculated and act as additional diagnostics inside the AI regressor. There is a very low or null contribution of weak neutral C,N,O permitted lines (except for a few cases at 320 days). This is a consequence of our focus on evolved shells (when those transitions are usually fainter) and the brightness-driven selection method (see in [Section 2.2](#)), which does not impose prior knowledge about line formation but rather ranks the brightest ones.

### 3.3. *Machine Learning and Dimensionality Reduction Probe*

As a follow-up to our diagnostic line sets, we built a [Random Forest Regressor](#) epoch-wise model for the post-eruption ages with complete Parameter-Space variable coverage. The goal is to constrain the physical parameters and abundances for each age using the information from the PCA-selected line sets. Other spectroscopic multivariate problems have been tackled with RFRs trained on the complete available data set (e.g. [Hong et al. 2025](#); [Li et al. 2025](#)). In the present case, the limited sampling of parameters represents a computational limitation. On the other hand, a large number of observables (normalized line fluxes) are available for each nova age.

The RFR prediction capability is evaluated by the mean absolute error (MAE), calculated from the differences between the parameter values found by the RFR (using the line fluxes only) and their actual model values, as set in the database spectrum synthesis. From now on, we will refer to the RFR trained with the Epoch-Selection 100 lines as the *Goldstandard* (in terms of spectral information available) and compare its performance with the [Top 10](#) PCA-based (refer to [Table 4](#)) regressor model. [Table 6](#) Summarize the MAE ranges for both regressors across all ages, clearly showing that the reduction in the number of lines used in the training from the 100 brightest ones to the 10 identified as most important by the PCA leads to slightly higher errors (especially for C,N,O abundance estimation) for most physical parameters; nevertheless, the metrics achieved are still lower than any other spectral regression method available, allowing us to conclude that the PCA line selection was successful, meaning a dimensionality reduction from 240 to 10 lines. Such an evaluation of regression performance with spectral information can only be conducted using a homogeneous synthetic database in which a large number of lines are available. Thanks to the previous PCA selection, it boils down to an observable line set.

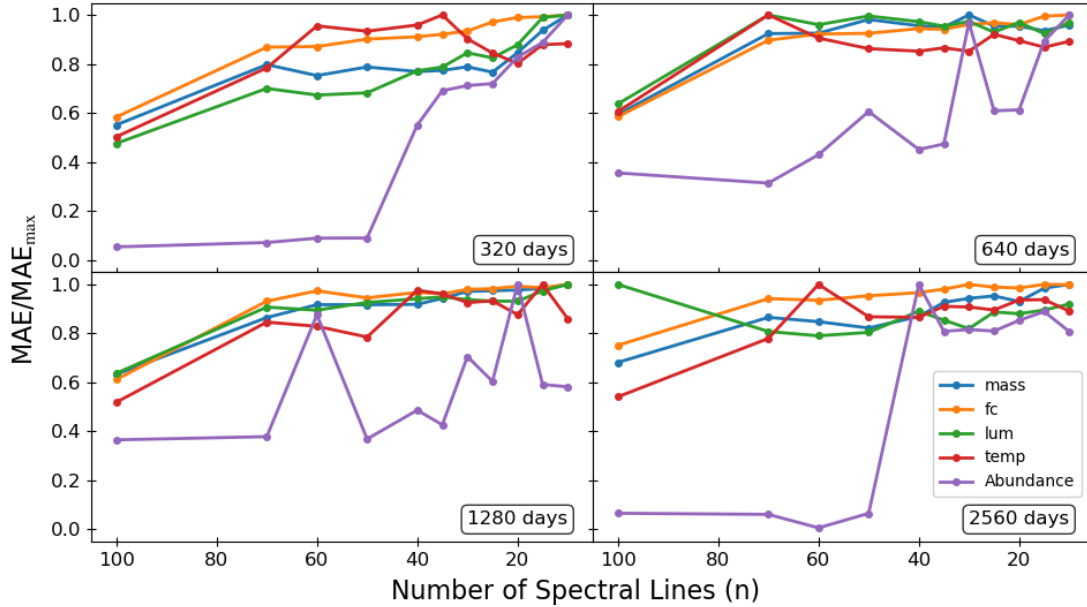
Besides the excellent overall performance of both regressor classes mentioned above, higher uncertainties are found in estimating the condensed fraction, with systematically lower global variance explained by the model in comparison to the other physical variables. This limited performance does not prevent the regressor models from achieving a mean error of 30% or less for the condensed mass fraction estimation, which seems to be a promising result for future improvement.

For a more detailed view, [Figure 2](#) shows the epoch-wise MAE evolution with the decrease in the number of lines available for regressor training. It can be seen that,

**Table 6.** MAE Ranges: Goldstandard vs Top 10 Lines (All Ages)

Parameter	Goldstandard		Top 10 Lines	
	min	max	min	max
Mass ( $M_{\odot}$ )	$1.03 \times 10^{-5}$	$1.16 \times 10^{-5}$	$1.20 \times 10^{-5}$	$1.43 \times 10^{-5}$
fc	0.1357	0.1555	0.1575	0.1725
Luminosity (dex)	0.169	0.191	0.133	0.267
Temperature (K)	6783.0	12997	10367	17436
C,N,O abundance (dex)	0.0066	0.0177	0.0127	0.2038

NOTE— MAE ranges across all models and all epochs (320-2560 days). The top 10 lines approach shows slightly higher errors for most parameters but maintains reasonable performance, demonstrating the efficacy of the diagnostic line selection.

**Figure 2.** Normalized Mean Absolute Error achieved for the Goldstandard (100 lines) and Top  $n$  RFR models

with the exception of the C,N,O abundance diagnosis, the multi-regressor dimensionality reduction, guided by the PCA, results in an evaluation metric degradation of no more than twice as large. Some grid variables even had increased local performance compared to larger  $n$  regressors. The abundance retrieval shows some instability in the trend for some epochs, but no more than a threefold increase is seen.

As a sanity check, we evaluated whether the bright Epoch-selection of 100 lines indeed does not limit the mapping capability of the AI models. For this purpose, for

each post-eruption age, we built an RFR trained first using the entire nova Spectral-Space of 240 lines and compared its evaluation metrics with those of a regressor built with the respective 100 lines in Epoch-Selection. No significant difference was noted between the optimal models' performance trained with both line sets.

### 3.4. *Simulating Observations*

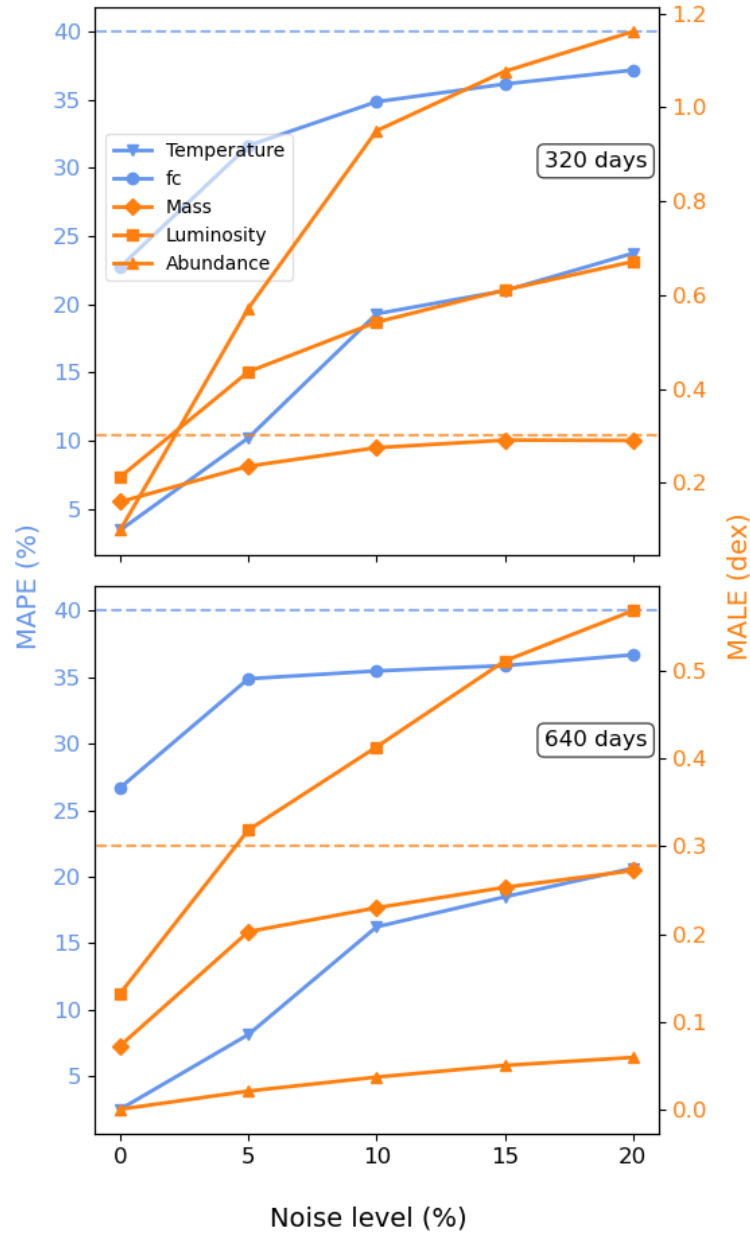
As a final test of the framework's predictive power, we compute the median *MAPE* and *MALE* for increasing levels of Gaussian noise added to the line intensities. These metrics quantify the expected predictive uncertainty when applying our regressor to observational data. Specifically, the *MAPE* provides a percentage-based measure of accuracy for grid linear variables (namely T and fc), while the *MALE* (expressed in dex) accounts for the order-of-magnitude variations inherent to grid logarithmic variables (M, L, and C,N,O abundance). By evaluating these metrics when using noisy line ratios, we test the robustness of the Top 10 lines regressor model, demonstrating its ability to maintain reliable parameter retrieval.

Figure 3 shows the Top 10' performance metrics of the two earliest nebular phases of the NSDB; the behavior is the same for the two latest phases: even with a simulated 20% flux error, a safe upper margin for exploration, the regressor is able to retrieve the central source temperature, shell condensed fraction, and ejected mass within 40% and 0.3 dex median uncertainties, which demonstrates the excellent regression power of this framework even with noisy data.

Concerning the luminosity and abundance regression, the first has the greatest uncertainty among the Parameter-Space, with an upper limit across post-eruption ages of 0.7 dex. While this level of median error is somewhat greater than what some would consider acceptable, it is worth noting that this value is slightly above half of the grid's step, matching the expected level of type B uncertainty.

Finally, the abundance regression presents two distinct behaviors: at the two intermediate nebular ages, the regression was virtually perfect, achieving an uncertainty smaller than 0.06 dex. On the other hand, at 320 and 2560 days, the uncertainty is enhanced to 1.16 and 0.67 dex, respectively. Despite these values not being far from the errors of current methods', the discrepancy in performance between these ages draws attention, showing that the method behaves differently depending on the shell physical conditions.

These results, along with the possibility of automating the framework constructed here, encourage us to improve the NSDB grid's resolution and add more parameters to better describe the white dwarf-shell system, such as an anisotropic radiation field component from an accretion disk and more detailed mass distribution abstractions. In addition to increasing the number of synthetic conditions per post-eruption age, the retrieval capability of the regressor may be further enhanced with additional nova observables, keeping in mind the application to targets from current and future spectroscopic synoptic surveys.



**Figure 3.** MAPE (left blue axis) and MALE (right orange axis) variables-wise with increasing simulated noise at 320 (upper plot) and 640 days (bottom plot). The dashed lines represents 40% (blue) and 0.3 *dex* (orange) uncertainties.

#### 4. CONCLUSIONS

The Nova Synthetic Data Base, the first publicly available database of synthetic spectra for classical novae, is presented here. Generated with the CLOUDY based code RAINY3D, this database contains 875+547 nova remnant models with emission predicted from near-UV to the NIR. The grids are constructed over a range of physical parameters that cover the most commonly reported values in the literature for classical

novae in nebular phase. This kind of homogeneous grid, built with state-of-the-art photoionization models, is essential for the validation of robust multivariate and AI analysis methods, allowing for the development of multi-regressor machine learning algorithms with controlled physical data.

The framework’s first step is to establish the eigenspectra for dimension reduction. The PCA analysis was carried out to construct a representative basis on which the spectroscopic variance can be related to the physical properties of the white dwarf-shell system mapped within the NSDB.

With a new maximum variance basis, the importance level of spectral lines for the retrieval of a grid’s variable could be derived. The diagnostic significance rank is built by establishing a safe correlation threshold and the weight of a line in the description of eigenspectra; ultimately, this results in an efficient reduction of dimensionality from hundreds of predicted spectral lines to a restricted [observable set](#), achievable only with the variance-focused PCA method.

With the most meaningful information derived from PCA, a Random Forest Regressor was built for each post-eruption age. The physical prediction capability is high, with the Mean Absolute Error (MAE) below grid sampling intervals for all derived parameters for the shell and central source. Comparing the regression metrics of the full line set and the most diagnostically capable ones, only a slight increase in error is observed, which still compares to or surpasses typical photoionization derived uncertainties.

The derived framework also proved robust, demonstrating remarkable regression power in the presence of input flux data noise, with median errors below 0.3 dex for the ejected mass, 0.7 dex for luminosity, 40% for the condensed mass fraction, and 25% for the central source temperature, even with substantial 20% flux uncertainty.

In light of these results, we propose the framework constructed here as a fully automatable spectral diagnostic method, suitable for large data sets available from current and future synoptic nova surveys. The extended proof of concept presented here also provides motivation to expand and improve the NSDB model grid.

1 This study was financed by CAPES process no. 8887.994579/2024-00 and by São  
 2 Paulo Research Foundation (FAPESP) under grant 2019/08341-8. MPD thanks  
 3 CNPq for support under grant #305033. The authors acknowledge the National Lab-  
 4 oratory for Scientific Computing (LNCC/MCTI,Brazil) for providing HPC resources  
 5 of the SDumont supercomputer, which have contributed to the research results re-  
 6 ported in this paper. The authors also thank Bruno Gerotti for his contribution to  
 7 the calculation of NSDB.

## APPENDIX

## A. THE SPECTRAL-SPACE NOVA LINE SELECTION

This appendix provides the full list of the 241 spectral lines predicted by the RAINY3D photoionization models as output for the NSDB grids. The complete spectral-space selection, including ion identification and wavelengths, is presented in [Table 7](#).

## B. BRIGHTEST 100 LINE SELECTIONS PER AGE

Epoch-Selections in increasing order of wavelength are shown in [Tables 8-13](#).

**Table 7.** Complete Spectral-Space selection of Nova lines.

Element	$\lambda$ ( $\lambda\text{\AA}$ )	Element	$\lambda$ ( $\lambda\text{\AA}$ )	Element	$\lambda$ ( $\lambda\text{\AA}$ )	Element	$\lambda$ ( $\lambda\text{\AA}$ )	Element	$\lambda$ ( $\lambda\text{\AA}$ )
He II	3203.04	Fe II	3227.74	Fe II	3255.89	Fe II	3277.12	Fe II	3281.29
[Ne III]	3342.18	[Ne v]	3345.99	[Fe VI]	3813.55	[Ne v]	3426.03	O VI	3434.00
[Fe VI]	3492.10	[Fe VI]	3555.61	[Fe VII]	3586.32	[Fe VI]	3662.50	Ca II	3706.02
[S III]	3721.63	[O II]	3726.03	H I	3734.36	Ca II	3736.90	H I	3750.15
[Fe VII]	3758.92	H I	3770.63	H I	3797.89	H I	3835.38	He II	3857.96
[Ne III]	3868.76	He I	3888.63	Al II	3900.67	He II	3923.37	Ca II	3933.66
[Ne III]	3967.47	Ca II	3968.47	H I	3970.07	[Fe XI]	3986.88	[Fe v]	4026.12
He I	4026.20	[S II]	4068.60	[Fe v]	4071.24	[S II]	4076.35	H I	4101.73
He I	4143.76	Fe II	4178.96	[Fe v]	4180.59	C III	4187.00	[Fe v]	4229.27
Fe II	4233.17	[Fe II]	4243.97	C II	4267.00	[Fe II]	4287.39	Fe II	4305.89
H I	4340.46	Fe II	4352.78	[Fe II]	4359.33	[O III]	4363.21	Fe II	4384.32
He I	4387.93	Fe II	4413.78	[Fe II]	4416.27	He I	4437.55	[Fe II]	4457.94
He I	4471.49	Mg II	4481.15	Fe II	4492.63	Fe II	4514.90	He II	4541.46
Fe II	4555.89	Mg I	4571.10	Fe II	4584.00	Fe II	4629.34	N III	4641.00
[Fe III]	4658.01	C IV	4659.00	He II	4685.64	[Fe III]	4701.62	He I	4713.03
[Ar IV]	4740.12	[Fe III]	4754.64	[Fe II]	4814.53	H I	4861.33	[Fe III]	4881.12
Fe VII	4893.37	He I	4921.93	Fe II	4923.93	[Ca VII]	4939.56	[Fe VII]	4942.48
N v	4945.00	[O III]	4958.91	[Fe VI]	4967.15	[Fe VI]	4971.72	[Fe VII]	4988.55
[O III]	5006.84	He I	5015.68	Fe II	5018.44	He I	5047.64	[Fe VI]	5145.76
[Fe II]	5158.78	[Fe VII]	5158.89	Fe II	5169.03	[Fe VI]	5176.05	[Fe II]	5261.62
[Fe III]	5270.40	Fe II	5273.35	[Fe II]	5276.00	[Fe VII]	5276.38	Fe II	5284.11
O VI	5291.00	[Fe XIV]	5303.01	[Ca v]	5309.11	Fe II	5316.62	Fe II	5362.87
He II	5411.37	Fe II	5414.07	[Fe VI]	5424.23	Fe II	5425.26	Fe II	5527.34
[Ar X]	5534.02	Fe II	5534.85	[O I]	5577.34	[Ca VII]	5618.76	[Fe VI]	5631.08
[Fe VI]	5676.96	N II	5679.00	[Fe VII]	5720.71	N II	5755.00	Ca VI	5765.38
He I	5875.64	Na I	5895.92	Fe II	5991.38	Fe II	6084.11	[Fe VII]	6086.97
[Ca v]	6086.37	He II	6233.61	Fe II	6248.06	[O I]	6300.30	He II	6310.64
[S III]	6312.06	Si II	6347.11	[O I]	6363.78	Si II	6371.37	[Fe x]	6374.54
[Ar v]	6435.12	[N II]	6548.05	He II	6559.91	H I	6562.81	[N II]	6583.45
He I	6678.15	He II	6682.98	Li I	6707.76	[S II]	6716.44	[S II]	6730.82
He II	6890.67	[Ar v]	7005.83	He I	7065.22	[Ar III]	7135.79	[Fe II]	7155.16
[Ar IV]	7170.70	He II	7177.28	Ca II	7234.34	[Ar IV]	7237.77	[Ar IV]	7263.33
He I	7281.35	Ca II	7291.47	Fe II	7306.65	O II	7329.67	[O II]	7330.73
N I	7452.00	N IV	7582.00	He II	7592.50	N IV	7703.00	O IV	7713.00
[S I]	7725.05	[Ar III]	7751.11	O I	7773.00	[P II]	7875.99	[Fe XI]	7891.87
Mg II	7896.04	[Mn IX]	7968.49	N I	8212.00	He II	8236.51	O I	8446.25
Ca II	8498.02	H I	8502.44	Ca II	8542.09	H I	8545.34	H I	8598.35
Ca II	8662.14	H I	8664.98	N I	8692.99	[Cl I]	8727.12	H I	8759.42

**Table 8.** Epoch-Selection for 80 days age.

Element	$\lambda$ ( $\lambda\text{\AA}$ )	Element	$\lambda$ ( $\lambda\text{\AA}$ )	Element	$\lambda$ ( $\lambda\text{\AA}$ )	Element	$\lambda$ ( $\lambda\text{\AA}$ )	Element	$\lambda$ ( $\lambda\text{\AA}$ )
He II	3203.04	[Ne III]	3342.18	[Ne V]	3345.99	[Ne V]	3426.03	O VI	3434.00
[Fe VI]	3492.10	[Fe VI]	3555.61	[Fe VII]	3586.32	[Fe VI]	3662.50	H I	3734.36
H I	3750.15	[Fe VII]	3758.92	H I	3770.63	H I	3797.89	[Fe VI]	3813.55
H I	3835.38	[Ne III]	3868.76	He I	3888.63	He II	3923.37	[Ne III]	3967.47
H I	3970.07	[Fe XI]	3986.88	He I	4026.20	[Fe V]	4071.24	H I	4101.73
[Fe V]	4180.59	H I	4340.46	[O III]	4363.21	He I	4387.93	He I	4471.49
He II	4541.46	C IV	4659.00	He II	4685.64	He I	4713.03	[Ar IV]	4740.12
Fe VII	4893.37	He I	4921.93	[Ca VII]	4939.56	[Fe VII]	4942.48	N V	4945.00
[O III]	4958.91	[Fe VI]	4967.15	[Fe VII]	4988.55	[O III]	5006.84	He I	5015.68
[Fe VI]	5145.76	[Fe VII]	5158.89	[Fe VI]	5176.05	[Fe VII]	5276.38	O VI	5291.00
[Ca V]	5309.11	He II	5411.37	[Fe VI]	5424.23	[Ar X]	5534.02	[Ca VII]	5618.76
[Fe VI]	5631.08	[Fe VI]	5676.96	[Fe VII]	5720.71	[N II]	5755.00	He I	5875.64
[Ca V]	6086.37	[Fe VII]	6086.97	[S III]	6312.06	[Fe X]	6374.54	[Ar V]	6435.12
He II	6559.91	H I	6562.81	He I	6678.15	He II	6682.98	He II	6890.67
[Ar V]	7005.83	He I	7065.22	[Ar III]	7135.79	[Ar IV]	7170.70	He II	7177.28
He I	7281.35	He II	7592.50	[Fe XI]	7891.87	[Mn IX]	7968.49	He II	8236.51
H I	8750.43	H I	8862.74	H I	9014.87	H I	9228.97	He II	9344.62
[S III]	9530.62	H I	9545.93	H I	10049.30	He II	10123.30	He I	10830.30
H I	10938.00	H I	12818.00	H I	18174.00	H I	18751.00	H I	19445.40
[Al IX]	20444.40	He I	20581.30	H I	21655.10	[Ca VIII]	23211.70	[Si VII]	24807.10

## REFERENCES

- Abraham, Z., Takeda, L., Beaklini, P. P. B., et al. 2024, *MNRAS*, 527, 7482, doi: [10.1093/mnras/stad3647](https://doi.org/10.1093/mnras/stad3647)
- Asplund, M., Grevesse, N., Sauval, A. J., & Scott, P. 2009, *Annual Review of Astronomy and Astrophysics*, 47, 481, doi: <https://doi.org/10.1146/annurev.astro.46.060407.145222>
- Borisov, S., Prantzos, N., & Charbonnel, C. 2024, *A&A*, 691, A142, doi: [10.1051/0004-6361/202451321](https://doi.org/10.1051/0004-6361/202451321)
- Breiman, L. 2001, *Machine Learning*, 45, 5, doi: [10.1023/A:1010933404324](https://doi.org/10.1023/A:1010933404324)
- Devore, J. L. 2011, *Probability and Statistics for Engineering and the Sciences*, 8th edn. (Brooks/Cole, Cengage Learning). <https://www.cengage.com/c/probability-and-statistics-for-engineering-and-the-sciences-8th-edition/>
- Diaz, M. P., Abraham, Z., Ribeiro, V. A. R. M., Beaklini, P. P. B., & Takeda, L. 2018, *MNRAS*, 480, L54, doi: [10.1093/mnras/sly121](https://doi.org/10.1093/mnras/sly121)
- Diaz, M. P., Williams, R. E., Luna, G. J., Moraes, M., & Takeda, L. 2010, *The Astronomical Journal*, 140, 1860, doi: [10.1088/0004-6256/140/6/1860](https://doi.org/10.1088/0004-6256/140/6/1860)

**Table 9.** Epoch-Selection for 160 days age.

Element	$\lambda$ ( $\lambda\text{\AA}$ )	Element	$\lambda$ ( $\lambda\text{\AA}$ )	Element	$\lambda$ ( $\lambda\text{\AA}$ )	Element	$\lambda$ ( $\lambda\text{\AA}$ )	Element	$\lambda$ ( $\lambda\text{\AA}$ )
He II	3203.04	[Ne III]	3342.18	[Ne V]	3345.99	[Ne V]	3426.03	O VI	3434.00
[Fe VI]	3492.10	[Fe VI]	3555.61	[Fe VII]	3586.32	[Fe VI]	3662.50	[S III]	3721.63
H I	3734.36	H I	3750.15	[Fe VII]	3758.92	H I	3770.63	H I	3797.89
[Fe VI]	3813.55	H I	3835.38	He II	3857.96	[Ne III]	3868.76	He I	3888.63
He II	3923.37	[Ne III]	3967.47	H I	3970.07	[Fe XI]	3986.88	He I	4026.20
[Fe V]	4071.24	H I	4101.73	[Fe V]	4180.59	H I	4340.46	[O III]	4363.21
He I	4471.49	He II	4541.46	C IV	4659.00	He II	4685.64	He I	4713.03
[Ar IV]	4740.12	Fe VII	4893.37	He I	4921.93	[Ca VII]	4939.56	[Fe VII]	4942.48
N V	4945.00	[O III]	4958.91	[Fe VI]	4967.15	[Fe VII]	4988.55	[O III]	5006.84
He I	5015.68	[Fe VI]	5145.76	[Fe VII]	5158.89	[Fe VI]	5176.05	[Fe VII]	5276.38
O VI	5291.00	[Fe XIV]	5303.01	[Ca V]	5309.11	He II	5411.37	[Fe VI]	5424.23
[Ar X]	5534.02	[Ca VII]	5618.76	[Fe VI]	5631.08	[Fe VI]	5676.96	[Fe VII]	5720.71
[N II]	5755.00	He I	5875.64	[Ca V]	6086.37	[Fe VII]	6086.97	[S III]	6312.06
[Fe X]	6374.54	[Ar V]	6435.12	[N II]	6548.05	He II	6559.91	H I	6562.81
[N II]	6583.45	He I	6678.15	He II	6682.98	He II	6890.67	[Ar V]	7005.83
He I	7065.22	[Ar III]	7135.79	He II	7177.28	He I	7281.35	He II	7592.50
[Fe XI]	7891.87	[Mn IX]	7968.49	He II	8236.51	H I	9014.87	[S III]	9068.62
H I	9228.97	He II	9344.62	[S III]	9530.62	H I	9545.93	H I	10049.30
He II	10123.30	He I	10830.30	H I	10938.00	H I	12818.00	H I	18751.00
[Al IX]	20444.40	He I	20581.30	H I	21655.10	[Ca VIII]	23211.70	[Si VII]	24807.10

Ercolano, B., Barlow, M. J., Storey, P. J., & Liu, X.-W. 2003, *Monthly Notices of the Royal Astronomical Society*, 340, 1136, doi: [10.1046/j.1365-8711.2003.06371.x](https://doi.org/10.1046/j.1365-8711.2003.06371.x)

Ferland, G. J., Porter, R. L., van Hoof, P. A. M., et al. 2013, *The Astrophysical Journal Supplement Series*, 208, 19, doi: [10.1088/0067-0049/208/1/19](https://doi.org/10.1088/0067-0049/208/1/19)

Gehrz, R. D., Truran, J. W., Williams, R. E., & Starrfield, S. 1998, *PASP*, 110, 3, doi: [10.1086/316107](https://doi.org/10.1086/316107)

Gruenwald, R., Viegas, S. M., & Broguière, D. 1997, *The Astrophysical Journal*, 480, 283, doi: [10.1086/303941](https://doi.org/10.1086/303941)

Hong, J., Kirby, E. N., Tang, T. M., et al. 2025, *ApJ*, 989, 48,

doi: [10.3847/1538-4357/ade679](https://doi.org/10.3847/1538-4357/ade679)

Ivezić, Ž., Connolly, A. J., VanderPlas, J. T., & Gray, A. 2019, *Statistics, data mining, and machine learning in astronomy* (Princeton University Press)

Li, Q., Xiong, J., Li, J., et al. 2025, *ApJS*, 276, 19, doi: [10.3847/1538-4365/ad8fa9](https://doi.org/10.3847/1538-4365/ad8fa9)

M. Moraes, M. D. 2011, *Publications of the Astronomical Society of the Pacific*, 123, 844, doi: [10.1086/660906](https://doi.org/10.1086/660906)

Maoz, D., Mannucci, F., & Nelemans, G. 2014, *Annual Review of Astronomy and Astrophysics*, 52, 107, doi: [10.1146/annurev-astro-082812-141031](https://doi.org/10.1146/annurev-astro-082812-141031)

**Table 10.** Epoch-Selection for 320 days age.

Element	$\lambda$ ( $\lambda\text{\AA}$ )	Element	$\lambda$ ( $\lambda\text{\AA}$ )	Element	$\lambda$ ( $\lambda\text{\AA}$ )	Element	$\lambda$ ( $\lambda\text{\AA}$ )	Element	$\lambda$ ( $\lambda\text{\AA}$ )
He II	3203.04	[Ne v]	3345.99	[Ne v]	3426.03	O VI	3434.00	[Fe VI]	3492.10
[Fe VI]	3555.61	[Fe VII]	3586.32	[Fe VI]	3662.50	[O II]	3726.03	H I	3734.36
H I	3750.15	[Fe VII]	3758.92	H I	3770.63	H I	3797.89	[Fe VI]	3813.55
H I	3835.38	[Ne III]	3868.76	He I	3888.63	[Ne III]	3967.47	H I	3970.07
[Fe XI]	3986.88	He I	4026.20	[Fe V]	4071.24	H I	4101.73	[Fe V]	4180.59
C III	4187.00	C II	4267.00	H I	4340.46	[O III]	4363.21	He I	4471.49
He II	4541.46	N III	4641.00	C IV	4659.00	He II	4685.64	[Ar IV]	4740.12
Fe VII	4893.37	[Ca VII]	4939.56	[Fe VII]	4942.48	N V	4945.00	[O III]	4958.91
[Fe VI]	4967.15	[Fe VII]	4988.55	[O III]	5006.84	He I	5015.68	[Fe VI]	5145.76
[Fe VII]	5158.89	[Fe VI]	5176.05	[Fe VII]	5276.38	O VI	5291.00	[Fe XIV]	5303.01
[Ca V]	5309.11	He II	5411.37	[Fe VI]	5424.23	[Ar X]	5534.02	[Ca VII]	5618.76
[Fe VI]	5631.08	[Fe VI]	5676.96	N II	5679.00	[Fe VII]	5720.71	[N II]	5755.00
He I	5875.64	[Ca V]	6086.37	[Fe VII]	6086.97	[S III]	6312.06	[Fe X]	6374.54
[Ar V]	6435.12	[N II]	6548.05	He II	6559.91	H I	6562.81	[N II]	6583.45
He I	6678.15	[Ar V]	7005.83	He I	7065.22	[Ar III]	7135.79	He II	7177.28
O II	7329.67	[O II]	7330.73	N IV	7582.00	He II	7592.50	N IV	7703.00
O IV	7713.00	O I	7773.00	[Fe XI]	7891.87	[Mn IX]	7968.49	He II	8236.51
N I	8692.00	[S III]	9068.62	O I	9264.00	He II	9344.62	[S III]	9530.62
H I	9545.93	H I	10049.30	He II	10123.30	He I	10830.30	H I	10938.00
H I	12818.00	H I	18751.00	[Al IX]	20444.40	[Ca VIII]	23211.70	[Si VII]	24807.10

McKinney, W. 2010, Proceedings of the 9th Python in Science Conference, 445, 51, doi: [10.25080/Majora-92bf1922-00a](https://doi.org/10.25080/Majora-92bf1922-00a)

Moraes, M., & Diaz, M. 2009, The Astronomical Journal, 138, 1541, doi: [10.1088/0004-6256/138/6/1541](https://doi.org/10.1088/0004-6256/138/6/1541)

Murtagh, F., & Heck, A. 2012, Multivariate Data Analysis, 4th edn., Springer Series in Statistics (Springer Science & Business Media), doi: [10.1007/978-1-4614-7163-5](https://doi.org/10.1007/978-1-4614-7163-5)

Osterbrock, D. E., & Ferland, G. J. 2006, Astrophysics of Gaseous Nebulae and Active Galactic Nuclei, 2nd edn. (University Science Books), doi: [10.48550/arXiv.astro-ph/0606171](https://doi.org/10.48550/arXiv.astro-ph/0606171)

Pedregosa, F., Varoquaux, G., Gramfort, A., et al. 2011, Journal of Machine Learning Research, 12, 2825

Perlmutter, S., Aldering, G., Goldhaber, G., et al. 1999, ApJ, 517, 565, doi: [10.1086/307221](https://doi.org/10.1086/307221)

Rauch, T. 2003, A&A, 403, 709, doi: [10.1051/0004-6361:20030412](https://doi.org/10.1051/0004-6361:20030412)

Riess, A. G., Filippenko, A. V., Challis, P., et al. 1998, AJ, 116, 1009, doi: [10.1086/300499](https://doi.org/10.1086/300499)

Slavin, A. J., O'Brien, T. J., & Dunlop, J. S. 1995, Monthly Notices of the Royal Astronomical Society, 276, 353, doi: [10.1093/mnras/276.2.353](https://doi.org/10.1093/mnras/276.2.353)

**Table 11.** Epoch-Selection for 640 days age.

Element	$\lambda$ ( $\lambda\text{\AA}$ )	Element	$\lambda$ ( $\lambda\text{\AA}$ )	Element	$\lambda$ ( $\lambda\text{\AA}$ )	Element	$\lambda$ ( $\lambda\text{\AA}$ )	Element	$\lambda$ ( $\lambda\text{\AA}$ )
He II	3203.04	[Ne v]	3345.99	[Ne v]	3426.03	O VI	3434.00	[Fe VI]	3492.10
[Fe VI]	3555.61	[Fe VII]	3586.32	[Fe VI]	3662.50	H I	3734.36	H I	3750.15
[Fe VII]	3758.92	H I	3770.63	H I	3797.89	[Fe VI]	3813.55	H I	3835.38
He II	3857.96	[Ne III]	3868.76	He I	3888.63	He II	3923.37	[Ne III]	3967.47
H I	3970.07	[Fe XI]	3986.88	He I	4026.20	[Fe V]	4071.24	H I	4101.73
[Fe V]	4180.59	C III	4187.00	C II	4267.00	H I	4340.46	[O III]	4363.21
He I	4471.49	He II	4541.46	N III	4641.00	C IV	4659.00	He II	4685.64
[Ar IV]	4740.12	Fe VII	4893.37	[Ca VII]	4939.56	[Fe VII]	4942.48	N V	4945.00
[O III]	4958.91	[Fe VI]	4967.15	[Fe VII]	4988.55	[O III]	5006.84	He I	5015.68
[Fe VI]	5145.76	[Fe VII]	5158.89	[Fe VI]	5176.05	[Fe VII]	5276.38	O VI	5291.00
[Fe XIV]	5303.01	[Ca V]	5309.11	He II	5411.37	[Fe VI]	5424.23	[Ar X]	5534.02
[Ca VII]	5618.76	[Fe VI]	5631.08	[Fe VI]	5676.96	N II	5679.00	[Fe VII]	5720.71
He I	5875.64	[Ca V]	6086.37	[Fe VII]	6086.97	[Fe X]	6374.54	[Ar V]	6435.12
[N II]	6548.05	He II	6559.91	H I	6562.81	[N II]	6583.45	He I	6678.15
He II	6682.98	He II	6890.67	[Ar V]	7005.83	He I	7065.22	He II	7177.28
N IV	7582.00	He II	7592.50	N IV	7703.00	O IV	7713.00	[Fe XI]	7891.87
[Mn IX]	7968.49	He II	8236.51	H I	8862.74	H I	9014.87	[S III]	9068.62
H I	9228.97	He II	9344.62	[S III]	9530.62	H I	9545.93	H I	10049.30
He II	10123.30	He I	10830.30	H I	10938.00	H I	12818.00	H I	18751.00
H I	19445.40	[Al IX]	20444.40	H I	21655.10	[Ca VIII]	23211.70	[Si VII]	24807.10

Starrfield, S., Truran, J. W., Sparks, W. M., & Arnould, M. 1978, *ApJ*, 222, 600, doi: [10.1086/156175](https://doi.org/10.1086/156175)

Takeda, L., Diaz, M., Campbell, R., & lyke, J. 2018, *Monthly Notices of the Royal Astronomical Society*, 473, 355, doi: [10.48550/arXiv.1709.01205](https://doi.org/10.48550/arXiv.1709.01205)

The pandas development team. 2023, *pandas: powerful Python data analysis toolkit, v2.1.4, 2.1.4*, Zenodo, doi: [10.5281/zenodo.10052348](https://doi.org/10.5281/zenodo.10052348)

Warner, B. 1995, *Cambridge Astrophysics Series, Vol. 28, Cataclysmic Variable Stars* (Cambridge University Press), doi: [10.1017/CBO9780511586491](https://doi.org/10.1017/CBO9780511586491)

Williams, R. E. 1992, *The Astrophysical Journal*, 392, 99

—. 1994, *The Astrophysical Journal*, 426, 279, doi: [10.1086/174060](https://doi.org/10.1086/174060)

Williams, R. E., Hamuy, M., Phillips, M. M., et al. 1991, *The Astrophysical Journal*, 376, 721, doi: [10.1086/170319](https://doi.org/10.1086/170319)

**Table 12.** Epoch-Selection for 1280 days age.

Element	$\lambda$ ( $\lambda\text{\AA}$ )	Element	$\lambda$ ( $\lambda\text{\AA}$ )	Element	$\lambda$ ( $\lambda\text{\AA}$ )	Element	$\lambda$ ( $\lambda\text{\AA}$ )	Element	$\lambda$ ( $\lambda\text{\AA}$ )
He II	3203.04	[Ne v]	3345.99	[Ne v]	3426.03	O VI	3434.00	[Fe VI]	3492.10
[Fe VI]	3555.61	[Fe VII]	3586.32	[Fe VI]	3662.50	H I	3734.36	H I	3750.15
[Fe VII]	3758.92	H I	3770.63	H I	3797.89	[Fe VI]	3813.55	H I	3835.38
He II	3857.96	[Ne III]	3868.76	He I	3888.63	He II	3923.37	[Ne III]	3967.47
H I	3970.07	[Fe XI]	3986.88	He I	4026.20	[Fe V]	4071.24	H I	4101.73
[Fe V]	4180.59	C III	4187.00	C II	4267.00	H I	4340.46	[O III]	4363.21
He I	4471.49	He II	4541.46	N III	4641.00	C IV	4659.00	He II	4685.64
[Ar IV]	4740.12	Fe VII	4893.37	He I	4921.93	[Ca VII]	4939.56	[Fe VII]	4942.48
N V	4945.00	[O III]	4958.91	[Fe VI]	4967.15	[Fe VII]	4988.55	[O III]	5006.84
[Fe VI]	5145.76	[Fe VII]	5158.89	[Fe VI]	5176.05	[Fe VII]	5276.38	O VI	5291.00
[Fe XIV]	5303.01	[Ca V]	5309.11	He II	5411.37	[Fe VI]	5424.23	[Ar X]	5534.02
[Ca VII]	5618.76	[Fe VI]	5631.08	[Fe VI]	5676.96	N II	5679.00	[Fe VII]	5720.71
He I	5875.64	[Ca V]	6086.37	[Fe VII]	6086.97	[Fe X]	6374.54	[Ar V]	6435.12
He II	6559.91	H I	6562.81	[N II]	6583.45	He I	6678.15	He II	6682.98
He II	6890.67	[Ar V]	7005.83	He I	7065.22	He II	7177.28	N IV	7582.00
He II	7592.50	N IV	7703.00	O IV	7713.00	[Fe XI]	7891.87	[Mn IX]	7968.49
He II	8236.51	H I	8750.43	H I	8862.74	H I	9014.87	[S III]	9068.62
H I	9228.97	He II	9344.62	[S III]	9530.62	H I	9545.93	H I	10049.30
He II	10123.30	He I	10830.30	H I	10938.00	H I	12818.00	H I	18751.00
H I	19445.40	[Al IX]	20444.40	H I	21655.10	[Ca VIII]	23211.70	[Si VII]	24807.10

**Table 13.** Epoch-Selection for 2560 days age.

Element	$\lambda$ ( $\lambda\text{\AA}$ )	Element	$\lambda$ ( $\lambda\text{\AA}$ )	Element	$\lambda$ ( $\lambda\text{\AA}$ )	Element	$\lambda$ ( $\lambda\text{\AA}$ )	Element	$\lambda$ ( $\lambda\text{\AA}$ )
He II	3203.04	[Ne v]	3345.99	[Ne v]	3426.03	O VI	3434.00	[Fe VI]	3492.10
[Fe VI]	3555.61	[Fe VII]	3586.32	[Fe VI]	3662.50	H I	3734.36	H I	3750.15
[Fe VII]	3758.92	H I	3770.63	H I	3797.89	[Fe VI]	3813.55	H I	3835.38
He II	3857.96	[Ne III]	3868.76	He I	3888.63	He II	3923.37	[Ne III]	3967.47
H I	3970.07	[Fe XI]	3986.88	He I	4026.20	[Fe V]	4071.24	H I	4101.73
[Fe V]	4180.59	C III	4187.00	H I	4340.46	[O III]	4363.21	He I	4471.49
He II	4541.46	N III	4641.00	C IV	4659.00	He II	4685.64	[Ar IV]	4740.12
Fe VII	4893.37	[Ca VII]	4939.56	[Fe VII]	4942.48	N V	4945.00	[O III]	4958.91
[Fe VI]	4967.15	[Fe VII]	4988.55	[O III]	5006.84	[Fe VI]	5145.76	[Fe VII]	5158.89
[Fe VI]	5176.05	[Fe VII]	5276.38	O VI	5291.00	[Fe XIV]	5303.01	[Ca V]	5309.11
He II	5411.37	[Fe VI]	5424.23	[Ar X]	5534.02	[Ca VII]	5618.76	[Fe VI]	5631.08
[Fe VI]	5676.96	[Fe VII]	5720.71	He I	5875.64	[Ca V]	6086.37	[Fe VII]	6086.97
[Fe X]	6374.54	[Ar V]	6435.12	He II	6559.91	H I	6562.81	He I	6678.15
He II	6682.98	He II	6890.67	[Ar V]	7005.83	He I	7065.22	He II	7177.28
N IV	7582.00	He II	7592.50	N IV	7703.00	O IV	7713.00	[Fe XI]	7891.87
[Mn IX]	7968.49	He II	8236.51	H I	8545.34	H I	8598.35	H I	8664.98
H I	8750.43	H I	8862.74	H I	9014.87	H I	9228.97	He II	9344.62
[S III]	9530.62	H I	9545.93	H I	10049.30	He II	10123.30	He I	10830.30
H I	10938.00	H I	12818.00	H I	18174.00	H I	18751.00	H I	19445.40
[Al IX]	20444.40	H I	21655.10	He II	21884.30	[Ca VIII]	23211.70	[Si VII]	24807.10